

Effects of domain walls in bilayer graphene in an external magnetic field

Nico S. Bäbler¹ and Kai Phillip Schmidt¹

¹*Lehrstuhl für Theoretische Physik I, Staudtstraße 7, FAU Erlangen-Nürnberg, D-91058 Erlangen, Germany*

We investigate bilayer graphene systems with layer switching domain walls separating the two energetically equivalent Bernal stackings in the presence of an external magnetic field. To this end we calculate quantum transport and local densities of three microscopic models for a single domain wall: a hard wall, a defect due to shear, and a defect due to tension. The quantum transport calculations are performed with a recursive Green's function method. Technically, we discuss an explicit algorithm for the separation of a system into subsystems for the recursion and we present an optimization of the well known iteration scheme for lead self-energies for sparse chain couplings. We find strong physical differences for the three different types of domain walls in the integer quantum Hall regime. For a domain wall due to shearing of the upper graphene layer there is a plateau formation in the magnetoconductance for sufficiently wide defect regions. For wide domain walls due to tension in the upper graphene layer there is only an approximate plateau formation with fluctuations of the order of the elementary conductance quantum σ_0 . A direct transition between stacking regions like for the hard wall domain wall shows no plateau formation and is therefore not a good model for either of the previously mentioned extended domain walls.

I. INTRODUCTION

Two dimensional quantum materials have risen in popularity quite dramatically in recent years. One aspect of this is the rapid progress in manufacturing processes [1] which allows the creation of a multitude of materials such as Van der Waals heterostructures [2]. Another aspect is the discovery of topological quantum phases like the topological insulator [3; 4], topological superconductors [5–7] as well strongly correlated intrinsic topological phases, which are relevant for topological quantum computing [8; 9] and potentially realized in fractional quantum Hall systems [10; 11] as well as in certain frustrated quantum magnets [12]. The first material proposed to be a topological insulator was single-layer graphene (SLG) [13], but the spin-orbit coupling required for graphene to exhibit a stable quantum spin Hall effect turned out to be too weak. Nevertheless, SLG has attracted an enormous scientific interest due its extraordinary mechanical [14] and electronic [15; 16] properties.

A variant of graphene which came into focus recently is bilayer graphene (BLG) [17–19], where most fascinatingly a correlated superconducting state has been identified experimentally in so-called twisted BLG [20–24]. Conventional BLG has many interesting physical properties which are often fundamentally different from its single-layer counterpart [25]. As an example, although BLG and SLG display an anomalous integer quantum Hall effect [26], the anomaly in BLG is quite different due to the quadratic low-energy band [27]. Indeed, the linear low-energy dispersion of SLG can be modeled by a Dirac Hamiltonian so that chiral quasiparticles induce a Berry phase of π leading naturally to conductance jumps of $4e^2/h$ in the magnetoconductance at zero energy. In contrast, the quadratic low-energy band of BLG gives rise to chiral quasiparticles inducing a Berry phase of 2π resulting in two-times larger conductance jumps of $8e^2/h$ in the magnetoconductance at charge neutrality.

Microscopically, BLG realizes a Bernal stacking [28]

so that two neighboring lattice sites from opposite layers correspond to different sublattices A and B. This leads to an exact two-fold degeneracy of the electronic structure with respect to AB and BA stacking which can be obtained from each other through inversion. As a consequence, BLG samples are typically not homogeneous but consist of a network of domains with AB or BA stacking. These domains are separated by defects which are created in the manufacturing process of BLG, e.g., with epitaxy [29; 30] or are separated due to the natural structure of slightly twisted BLG [21]. These extended defects, which cause a registry shift in BLG over 6 nm to 11 nm [31] are called layer switching walls (LSWs) (or alternatively either partial dislocations or strain solitons). There have been extensive studies on the precise nature of LSWs in real materials. The fact, that BLG is a two-dimensional material allows for a release of strain with out-of-plane buckling [32]. There are also restrictions on the physical stacking textures due to energetic considerations [33] and stacking boundary conditions.

In general, it is an interesting and important question to understand the impact of such LSWs on the physical properties of BLG. In an external electric field, topological modes protected from scattering are known to exist along these LSWs [34; 35]. Since samples usually contain many of these LSWs, applying an external electric field leads to the formation of networks of topological channels [36] due to the gap introduced into the electronic structure [37].

Another important aspect is the influence and role of LSWs on BLG in an external magnetic field or, more concretely, on the anomalous integer as well as fractional quantum Hall effect in this material. Recently, the physical properties of LSW networks in the presence of an external magnetic field have been studied [37; 38]. It is found that the presence of LSWs can lead to rich conductance features even in the single particle transport regime. It is argued that transport energy gaps in the meV regime are not caused by an electronic instability due to electronic interactions as typically assumed [39; 40], but simply due

to the structure of transport across LSWs and, in particular, due to “hot” charge carrying LSWs [41]. A similar argument for the presence of plateaus at fractional fillings [42–44] in BLG is made in [45], where arbitrary fractional plateaus are engineered in artificial SLG mosaics interconnected with metallic strips. It is proposed that there is an ambiguity in two-terminal transport experiments between the purely single-particle plateaus at fractional fillings due to LSWs and fractional plateaus originating from electron-electron interactions. However, this conclusion relies on a classical approximation of the couplings along linear LSWs. It is one purpose of our work to validate these findings by approaching the problem from a quantum perspective using an explicit real-space lattice model.

To this end we will use recursive Green’s function methods [46–51] to calculate magnetoconductance and the local density of states (LDOS) [52] for various BLG systems with LSWs. The systems used to model LSWs are two fairly realistic domain wall models, where shear and tension lead to the formation of an AB-BA domain wall [31], as well as an unrealistic hard wall model. Here we do not explicitly model out-of-plane buckling and simply describe these systems with a shear or stretch transformation of the upper graphene layer. We find relevant physical differences for these three different types of LSW in the integer quantum Hall regime. First, the hard wall model does not capture the essential physical properties for either of the other two extended domain walls due to shear or tension. Second, a domain wall due to shearing (tension) of the upper graphene layer yields an unexpected (approximate) plateau formation in the magnetoconductance for sufficiently wide defect regions.

This article is organized as follows. In Sect. II we introduce microscopic models for BLG with LSWs in the presence of an external magnetic field and we detail the relevant physical observables in Sect. III. Technical details on the implementation are given in Sect. IV while all obtained results are contained in Sect. V. Finally, we conclude in Sect. VI and present remaining open questions.

II. MODELS

We begin by describing a tight binding model of homogeneous BLG and three models of LSWs. The three models are BLG with hard layer switching wall (HLSW), shear layer switching wall (SLSW) and tension layer switching wall (TLSW) respectively. Afterwards, we discuss the transport setup used to determine the properties of the particular LSW models and the relevant observables.

1. Homogeneous blayer graphene

BLG is described generically by the simple tight binding model given in [53]. In the following we denote by $a_0 = a/\sqrt{3} \approx 0.142$ nm the nearest-neighbor distance be-

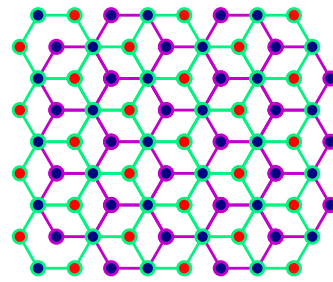


FIG. 1. Illustration of Bernal stacked BLG for a nearest-neighbour model. The green sheet is on top and the magenta sheet is in the bottom. The blue and red circles indicate the A and B sublattice respectively for both sheets.

tween carbon atoms of SLG and by $d_0 \approx 0.335$ nm the interlayer distance between vertically located atoms. In actual graphene, $a \approx 0.246$ nm, but all calculations are performed in units, such that $a = 1$. In addition, we omit the spin degree of freedom which gives only rise to a trivial degeneracy of 2. Consequently, we describe BLG with the following microscopic Hamiltonian

$$\mathcal{H}_{\text{BLG}} = - \sum_{\|\mathbf{r}_i - \mathbf{r}_j\| < D_c} t(\mathbf{r}_i, \mathbf{r}_j) \hat{c}_i^\dagger \hat{c}_j + \sum_i \mu_i \hat{c}_i^\dagger \hat{c}_i, \quad (1)$$

where \hat{c}_i^\dagger and \hat{c}_i are the usual fermionic creation and annihilation operators on the site with index i . The form of the onsite chemical potential μ_i will be discussed alongside the system parameters. The sum runs in principle over all pairs of sites, but we included a numerical cutoff D_c for practical calculations. The nearest-neighbor model is obtained for $D_c = a_0$. The hopping amplitudes are given by

$$-t(\mathbf{r}_i, \mathbf{r}_j) = V_{pp\pi} \left[1 - \left(\frac{\mathbf{d}_z}{\|\mathbf{d}\|} \right)^2 \right] + V_{pp\sigma} \left(\frac{\mathbf{d}_z}{\|\mathbf{d}\|} \right)^2, \quad (2)$$

where $\mathbf{d} = \mathbf{r}_i - \mathbf{r}_j$ is the atom-atom distance, $V_{pp\pi} = V_{pp\pi}^0 \exp[-(\|\mathbf{d}\| - a_0)/\delta]$ with $V_{pp\pi}^0$ the intralayer overlap integral between the nearest-neighbor atoms at a distance a_0 , and $V_{pp\sigma} = V_{pp\sigma}^0 \exp[-(\|\mathbf{d}\| - d_0)/\delta]$ with $V_{pp\sigma}^0$ the interlayer overlap integral at a distance d_0 . The explicit values $V_{pp\pi}^0 = -2.7$ eV and $V_{pp\sigma}^0 = 0.48$ eV for the overlap integrals can be obtained by fitting the low-energy dispersion of bulk graphite. Further, $\delta = 0.184a$ is the decay length of the overlap integral.

The Hamiltonian in Eq. (1) is quite general and can in principle model BLG at any twist angle, in particular the for BLG most relevant Bernal stacking which is illustrated in Fig. 1. Note that when not mentioned otherwise, we use a nearest-neighbor model with $D_c = a_0$ to describe the system.

For a constant external magnetic field perpendicular to the sheet plains of BLG, the Peierl’s substitution

$$t(\mathbf{r}_i, \mathbf{r}_j) \rightarrow t(\mathbf{r}_i, \mathbf{r}_j) \exp \left(-i \frac{e}{\hbar} \int_{\mathbf{r}_i}^{\mathbf{r}_j} \mathbf{A}(\mathbf{r}) d\mathbf{r} \right) \quad (3)$$

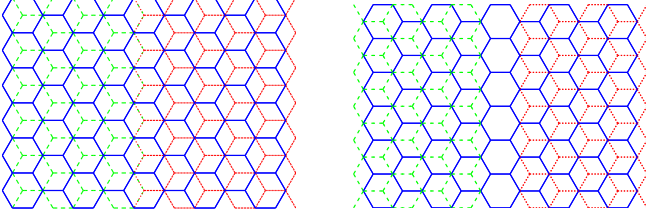


FIG. 2. Homogeneous and HLSW system. The lower layer is in blue and the upper layer is striped or dotted in red and green. On the left is a homogeneous AB stacked BLG system, which will be used as a reference system. On the right is the hard wall model for a LSW at the zigzag nanoribbon. The upper layer is decoupled, but any effective interaction may be of interest, in particular a fully coupled upper layer.

is chosen with a gauge that respects the translational symmetry of one of the electrodes which is usually a Landau gauge. The solution of this model for BLG in a perpendicular magnetic field yields then an anomalous integer quantum Hall effect (IQHE), which is calculated and discussed in Sect. V A.

2. Hard layer switching wall

The simplest model of a BLG system with an LSW is with a so-called hard wall. This established simplification of the LSW in BLG corresponds to an abrupt change between AB and BA Bernal stacking either parallel to the armchair or the zigzag nanoribbon. An illustration for the latter one is shown in comparison to a homogeneous BLG system in Fig. 2. Study of LSWs parallel to the zigzag nanoribbon is preferred since they are simpler to model and also encapsulate the topological properties of the stacking transition [54].

To define the Hamiltonian for a system with HLSW we split the system into a left side \mathcal{L} and a right side \mathcal{R} like in Fig. 2. The full Hamiltonian of a HLSW system is then given by

$$\mathcal{H}_{\text{HLSW}} = \mathcal{H}_{\text{BLG}}^{(\text{AB}, \mathcal{L})} + \mathcal{H}_{\text{BLG}}^{(\text{BA}, \mathcal{R})} + \mathcal{H}_{\text{HLSW}}^{(L)} + \mathcal{H}_{\text{HLSW}}^{(U)}, \quad (4)$$

in which $H_{\text{BLG}}^{(\text{AB}, \mathcal{L})}$ is the Hamiltonian for the BLG AB stacked bulk to the left and $H_{\text{BLG}}^{(\text{BA}, \mathcal{R})}$ for the BA stacked BLG bulk to the right as introduced in Eq. (1). The remaining two terms $\mathcal{H}_{\text{HLSW}}^{(L)}$ and $\mathcal{H}_{\text{HLSW}}^{(U)}$ describe the hopping elements between the left and right part and therefore represent the hard wall given by

$$H_{\text{HLSW}}^{(L)} = -t_{\text{LSW}}^{(L)} \sum_{\langle i, j \rangle} \left(a_i^{(L, \mathcal{L})} \right)^\dagger b_j^{(L, \mathcal{R})} + \text{h. c.} \quad (5)$$

$$H_{\text{HLSW}}^{(U)} = -t_{\text{LSW}}^{(U)} \sum_{\langle i, j \rangle} \left(a_i^{(U, \mathcal{L})} \right)^\dagger b_j^{(U, \mathcal{R})} + \text{h. c.} \quad (6)$$

Here $\left(\hat{a}_i^{(n, \kappa)} \right)^\dagger \left[\left(\hat{b}_i^{(n, \kappa)} \right)^\dagger \right]$ are the creation and annihilation operators for the A -sublattice [B -sublattice] of the layer $n \in \{L, U\}$ and side $\kappa \in \{\mathcal{L}, \mathcal{R}\}$ of the system.

In this work we always set the hopping integrals of the lower layer to be equal to the nearest-neighbor value $t_{\text{LSW}}^{(L)} \equiv t = 2.8 \text{ eV}$. In contrast, the one of the upper layer is a model parameter which we will tune. For $t_{\text{LSW}}^{(U)} = 0$, we call the upper layer *decoupled* while for $t_{\text{LSW}}^{(U)} = t$ the upper layer is called *fully coupled*.

A similar model can also be introduced as a simplification of an LSW parallel to the armchair nanoribbon. The armchair hard wall model is, however, not nearly as widely used in the literature and we will not study it in detail.

3. Shear and tensile layer switching wall

The hard wall model is adequate if properties are investigated which are related only to the topology of the material such as the formation of conducting channels in an external electric field. However, from an ab initio perspective, this is not clear for the case of an external magnetic field. A more realistic microscopic description of the domain walls is therefore important. The first step to model the LSW in BLG more realistically is to introduce an explicit finite lattice model for realistic LSW geometries. The natural deformation of the underlying lattice, that allows a smooth transition between domains is obtained by tensing or shearing a single layer of graphene. The existence of the layer transition due to such transformations has been experimentally confirmed in [31]. Let us stress that such a modeling of BLG, that is fixed tightly in two dimensions, is not expected to adequately describe a BLG system in which buckling occurs [32].

In order to explicitly define the shear and stretching transformation for BLG let us define first a general transformation. Given a lattice generated by primitive vectors $(\mathbf{p}_n)_{n=1, \dots, N}$ and basis vectors $(\mathbf{b}_m)_{m=1, \dots, M}$, denoted by

$$\mathcal{L} := \left\{ (\mathbf{p}_n)_{n=1, \dots, N}, (\mathbf{b}_m)_{m=1, \dots, M} \right\}, \quad (7)$$

we define its transformation due to a matrix \mathbf{M} by

$$\mathbf{M}\mathcal{L} := \left\{ (\mathbf{M}\mathbf{p}_n)_{n=1, \dots, N}, (\mathbf{M}\mathbf{b}_m)_{m=1, \dots, M} \right\}. \quad (8)$$

AB stacked BLG can then be described symbolically by the union of two lattices by $\mathcal{G}^{(AB)} := \mathcal{G}_L^{(AB)} \cup \mathcal{G}_U^{(AB)}$, where $\mathcal{G}_L^{(AB)}$ and $\mathcal{G}_U^{(AB)}$ correspond to the lower and upper layer of an AB stacked BLG respectively.

We are now in a position to define a sheared BLG lattice by $\mathcal{G}_s^{(AB)}(L_s) = \mathcal{G}_L^{(AB)} \cup \mathbf{S}(L_s)\mathcal{G}_U^{(AB)}$, where

$$\mathbf{S}(L_s) = \begin{pmatrix} 1 & 1/L_s \\ 0 & 1 \end{pmatrix} \quad (9)$$

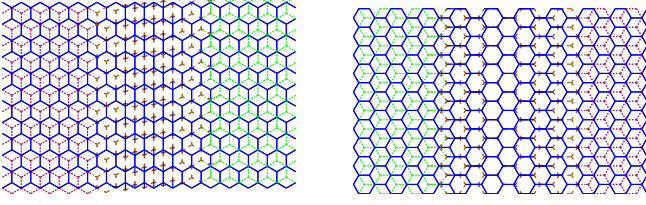


FIG. 3. Heterogeneous systems with LSWs containing BLG under shear (left) and tension (right). The lower layer is the solid blue lattice. The upper layer is in both cases either dotted or striped in green, orange and red respectively. Only the nearest-neighbour hoppings are shown.

is a shear transformation of the upper layer and L_s is the shear strength (or width). Similarly, tensed BLG is described by $\mathcal{G}_t^{(AB)}(L_t) = \mathcal{G}_L^{(AB)} \cup \mathbf{T}(L_t)\mathcal{G}_U^{(AB)}$, where

$$\mathbf{T}(L_t) = \begin{pmatrix} 1 & 0 \\ 0 & 1 + 1/L_t \end{pmatrix} \quad (10)$$

is a stretching transformation and L_t is the tensile strength (or width). Given the proper extent of the tensed region ($2aL_t/\sqrt{3}$) and of the sheared region ($aL_s/\sqrt{3}$), such a section of BLG transforms AB stacked BLG to BA stacked BLG. Equivalent lattices $\mathcal{G}_t^{(BA)}(L_t)$ and $\mathcal{G}_s^{(BA)}(L_s)$ can also be defined.

The previously defined lattices are shown in Fig. 3, where the SLSW and TLSW regions were chosen such that they exactly transform from AB stacked BLG bulk (left) to BA BLG bulk (right). It is clear by examining Fig. 3 that shear causes an LSW parallel to the armchair nanoribbon and tension an LSW parallel to the zigzag nanoribbon.

III. OBSERVABLES AND SYSTEM GEOMETRY

We start by defining the observables of interest. Then we describe the transport system setup and which system parameters are important for the calculation of the relevant observables.

These observables can be calculated using the usual nonequilibrium Green's function formalism. The retarded, advanced, and lesser Green's function are defined as

$$\begin{aligned} G_r(\mathbf{r}, t, \mathbf{r}', t') &= -i\theta(t - t') \langle \{ \Psi(\mathbf{r}, t), \Psi^\dagger(\mathbf{r}', t') \} \rangle \\ G_a(\mathbf{r}, t, \mathbf{r}', t') &= i\theta(t' - t) \langle \{ \Psi(\mathbf{r}, t), \Psi^\dagger(\mathbf{r}', t') \} \rangle \\ G^<(\mathbf{r}, t, \mathbf{r}', t') &= i \langle \Psi^\dagger(\mathbf{r}', t') \Psi(\mathbf{r}, t) \rangle \end{aligned} \quad (11)$$

and have interpretations as particle and hole propagators as well as correlators, respectively. $\Psi(\mathbf{r}, t)$ and $\Psi^\dagger(\mathbf{r}, t)$ are the usual field creation and destruction operators, that represent a particle field localized in space and will be replaced by their discrete counterparts for the lattice model. If the temperature of the system is zero,

$\langle \dots \rangle$ is evaluated with respect to the ground state and if the temperature is nonzero, it is evaluated with respect to the density matrix of the system. In this work, we will fully focus on the zero-temperature case. Given time homogeneity, the evaluation of the retarded and advanced quantities G_r and G_a simplify in the Fourier domain to $G_{r/a}(E) = \lim_{\eta \rightarrow 0} (E \pm i\eta - \mathcal{H}_S)^{-1}$ so that their evaluation corresponds to an inversion of the system Hamiltonian. The effect of the electrodes (leads) is modeled with an appropriate retarded self energy $\Sigma_{r,\text{lead}} = V_{S,\text{lead}} G_{r,\text{lead}} V_{S,\text{lead}}^\dagger$ obtained from the retarded surface Green's function of a semi-infinite chain $G_{r,\text{lead}}$ and coupling $V_{S,\text{lead}}$ of the chain to the system without electrodes (scattering region). For all systems under consideration in this article $G_a = G_r^\dagger$. The lesser Green's function can be obtained from the appropriate quantum kinetic equations, which are the fluctuation dissipation theorem and the Keldysh equation. These read

$$\Sigma^<(E) = -i \sum_n f(E, \mu_n) \left(G_a^{(n)}(E) - G_r^{(n)}(E) \right), \quad (12)$$

$$G^<(E) = G_r(E) \Sigma^<(E) G_a(E),$$

where the index (n) enumerates the electrodes at fixed chemical potentials μ_n and energy E , and $f(E, \mu_n)$ corresponds to the Fermi distribution describing the electron filling of the n th lead.

Given an algorithm for the evaluation of these Green's functions, most relevant observables may be evaluated. Two observables of particular interest are the conductance from electrode A to B

$$\sigma_{A \rightarrow B}(E) = \frac{2e}{\hbar} \text{tr} \left(\Gamma^{(A)} G_r \Gamma^{(B)} G_a \right) \quad (13)$$

with the coupling matrices $\Gamma^{(A/B)} = i \left(\Sigma_r^{(A/B)} - \Sigma_a^{(A/B)} \right)$ for the respective leads and the LDOS at site i

$$\rho_i(E) = \frac{1}{2\pi} \text{Im} \left(G_{ii}^<(E) \right) \quad (14)$$

in the zero temperature, zero bias limit at energy E . All equations presented above become matrix expressions in the case of a discrete lattice model and a calculation for large systems is possible with sophisticated algorithms as outlined in Sect. IV.

1. Hall bar geometry

The Hall bar geometry is an appropriate setup to examine systems in the IQHE regime and is particularly useful for the analysis of systems with LSWs. A sketch of the generic geometry of this measurement is shown in Fig. 4. It is a six-terminal device, that can resolve

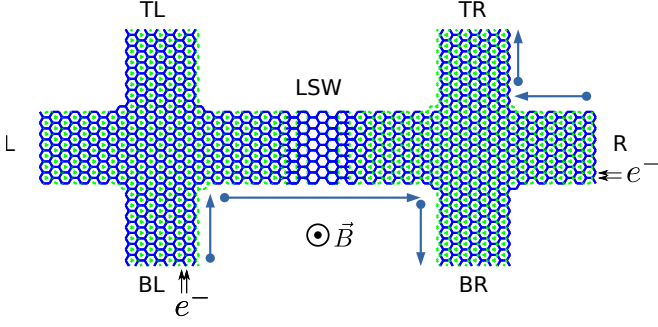


FIG. 4. Hall bar system with TLSW representing a general LSW. The lower graphene layer is solid blue and the upper layer is striped green. This is the generic system which will be used to discuss the IQHE in inhomogeneous or homogeneous BLG systems. It is a six-terminal structure with a lead connected to the system at each of the labels L (left), R (right), BL (bottom left), BR (bottom right), TL (top left) and TR (top right). The electron propagation in a homogeneous medium is indicated by blue arrows. The electron injection electrodes are also indicated with arrows.

the transport physics at the LSW, since transmitted and reflected modes can easily be distinguished by the structure of $\sigma_{BL \rightarrow BR}$ and $\sigma_{BL \rightarrow TL}$. The system displayed in Fig. 4 has an LSW due to tension in the upper layer in the center of the region. For other LSWs, the central region is replaced by the appropriate lattices as defined in Sect. III.

2. System parameters

We will use the following definitions and nomenclature for discussing the physical properties of BLG with layer switching domain walls:

- N_C/N_L : Number of sites in the conductance/LDOS calculation.
- D_C : Cutoff distance for hopping integrals in the upper layer and between layers in the LSW, where the graphene layers are thought of as being at the same distance as two nearest carbon atoms within a layer, $d_0 = a_0$. The couplings within the lower layer are always a nearest neighbor hopping.
- ϕ_{LDOS}^{-1} : Magnetic field value for the LDOS calculation. This value represents a physical magnetic field, but the Fermi energies for the transport calculations were chosen to be very large to suppress finite-size effects. For this reason the resulting magnetic fields would be unrealistically large. Thus this is kept as a parameter ϕ_{LDOS}^{-1} and not converted into absolute Tesla units.
- E_F : Fermi energy at which the calculations take place. All calculations are performed at zero temperature and zero bias, such that only the definition

of the Fermi energy and no other chemical potential is required. In all calculations in the main part of the paper we fixed the Fermi energy as $E_F = 0.35t \approx 0.95 \text{ eV}$.

Finally, we have added a random onsite disorder for all calculations corresponding to Gaussian noise with a width of $\Delta = 0.05t \approx 0.14 \text{ eV}$ around zero. This disorder is added to model the disorder required in real systems to observe the IQHE and to break unrealistic symmetries of the Hall bar geometry. The results however shall not depend vitally on the presence of such a disorder (calculations not shown).

IV. IMPLEMENTATION

The transport experiment simulation is essentially a recursive Green's function method implemented in C++. From the various particular implementation strategies of the bulk [49; 50; 55; 56] and lead self-energy calculation [57–59], a block Gaussian elimination solver for tridiagonal matrices [48] was chosen for the bulk recursion and a modified iteration [60] strategy was chosen for the lead self-energy calculation. Two particular additions to the implementation used for the results presented here are not discussed in these respective publications. They are presented including a summary of the algorithms from [48] and [60].

A. Calculation of lead self-energies

As mentioned previously, the electrodes (leads) are modeled by a semi-infinite chain. Calculation of the surface Green's function and thus the self-energy of such a chain can be efficiently performed by a chain decimation algorithm described in [60]. A short summary will be given here. To this end, define a periodically coupled chain with chain vertex (onsite) term $\mathbf{H}_{\text{chain}}$ and chain hopping (interaction) term $\mathbf{V}_{\text{chain}}$. Then recursive equations for a chain decimation with starting conditions $\epsilon_0 = \epsilon_0^s = \mathbf{H}_{\text{chain}}$ equal to the chain onsite Hamiltonian and $\alpha_0 = \beta_0^\dagger = \mathbf{V}_{\text{chain}}$ equal to the chain hopping Hamiltonian read

$$\begin{aligned} \alpha_i &= \alpha_{i-1}(\omega \mathbf{I} - \epsilon_{i-1})^{-1} \alpha_{i-1}, \\ \beta_i &= \beta_{i-1}(\omega \mathbf{I} - \epsilon_{i-1})^{-1} \beta_{i-1}, \\ \epsilon_i &= \epsilon_{i-1} + \alpha_{i-1}(\omega \mathbf{I} - \epsilon_{i-1})^{-1} \beta_{i-1} \\ &\quad + \beta_{i-1}(\omega \mathbf{I} - \epsilon_{i-1})^{-1} \alpha_{i-1}, \\ \epsilon_i^s &= \epsilon_{i-1}^s + \alpha_{i-1}(\omega \mathbf{I} - \epsilon_{i-1})^{-1} \beta_{i-1}, \end{aligned} \quad (15)$$

with $\omega = E + i\eta$ for the retarded solution which encodes a decimation of 2^n chain links after n iterations and the relevant chain surface Green's function becomes $G(\omega) = (\omega \mathbf{I} - \epsilon_n^s)^{-1}$ for a sufficiently large n .

An optimization to this algorithm which has not been discussed in the literature so far to the best of our knowledge is a reduction in matrix dimension of the Hamiltonian of the semi-infinite chain describing the lead. This reduction in matrix dimension is effective for chains, where the periodic coupling is sufficiently sparse. Such an optimization is effective since matrix inversion of sparse matrices does not produce sparse matrices in general and the expressions thus become dense after a few iteration steps. The size reduction is obtained by integrating the parts of the chain Hamiltonian, that do not participate in the periodic coupling into an effective Hamiltonian of reduced size including the interior parts of the chain.

For this purpose, we define the following quantities: The *left* section of the chain, which is periodically coupled to the previous chain link and the interior section, which is not coupled to the previous chain link. From these definitions, we obtain \mathbf{H}_L and \mathbf{H}_I , the respective subsystem matrices and \mathbf{V}_{IL} and \mathbf{V}_{LI} , the couplings between them (\mathbf{V}_{IL} is the coupling to the next period's *left* section). We also define the retarded Green's function \mathbf{G}_I of the interior subsystem. Using the notation from [60], the following starting parameters can be used:

$$\begin{aligned}\alpha_0 &= \beta_0^\dagger = \mathbf{V}_{LI} \mathbf{G}_I \mathbf{V}_{IL} \\ \epsilon_0 &= \mathbf{H}_L + \mathbf{V}_{LI} \mathbf{G}_I \mathbf{V}_{LI}^\dagger + \mathbf{V}_{IL}^\dagger \mathbf{G}_I \mathbf{V}_{IL} \\ \epsilon_0^s &= \mathbf{V}_{LI} \mathbf{G}_I \mathbf{V}_{LI}^\dagger.\end{aligned}\quad (16)$$

This effectively reduces the system size in the self-energy iteration from the dimension of an entire chain link d_{full} to the dimension of its *left* section d_{left} implying a reduction in complexity for all matrix operations performed from $\mathcal{O}(d_{\text{full}}^3)$ to $\mathcal{O}(d_{\text{left}}^3)$.

B. Calculation of select Green's function matrix elements

Given the definition $\mathbf{A} = \mathbf{E} - \mathbf{H} - \Sigma_{\text{lead}}$ of the transport problem we want to solve for matrix elements of $\mathbf{G} = \mathbf{A}^{-1}$. The reference [48] defines a modified Gaussian elimination, that uses a partition of \mathbf{A} into blocks \mathbf{a}_{nm} such that \mathbf{A} is block tridiagonal. To this end, a forward and backward elimination (left and right sweep in the more physics-oriented discussions of the recursive Green's function technique) are performed to obtain the matrices

$$\begin{aligned}d_{ii}^L &= \mathbf{a}_{ii} + \mathbf{c}_{i-1}^L \mathbf{a}_{i-1,i} & i &= 2, 3, \dots, n \\ \mathbf{c}_i^L &= -\mathbf{a}_{i+1,i} (\mathbf{d}_{ii}^L)^{-1} & i &= 1, 2, \dots, n-1 \\ d_{ii}^R &= \mathbf{a}_{ii} + \mathbf{c}_{i+1}^R \mathbf{a}_{i+1,i} & i &= n-1, \dots, 2, 1 \\ \mathbf{c}_i^R &= -\mathbf{a}_{i-1,i} (\mathbf{d}_{ii}^R)^{-1} & i &= n, \dots, 3, 2\end{aligned}\quad (17)$$

with $\mathbf{d}_{11}^L = \mathbf{a}_{11}^L$ and $\mathbf{d}_{nn}^R = \mathbf{a}_{nn}^R$, which can be combined to compute select matrix blocks of the retarded Green's function

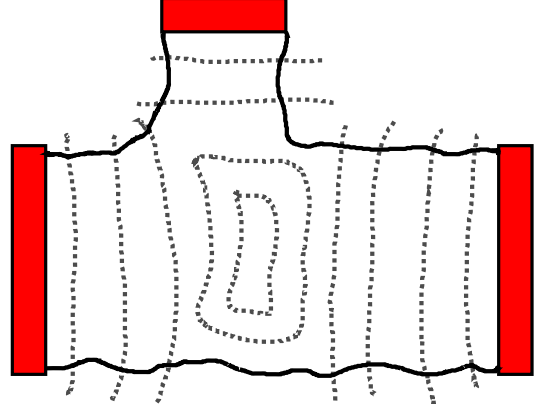


FIG. 5. Schematic depiction of a partition of a quite complicated geometry into appropriate subsystems such that the resulting Hamiltonian matrix is block tridiagonal with small blocks. Leads are shown in red and the dotted lines in grey show the lines that define the subsystems.

$$\begin{aligned}\mathbf{G}_{ii} &= (-\mathbf{a}_{ii} + \mathbf{d}_{ii}^L + \mathbf{d}_{ii}^R) \\ \mathbf{G}_{ij} &= \mathbf{G}_{ii} \mathbf{c}_{i+1}^R \mathbf{c}_i^R \dots \mathbf{c}_j^R & \text{for } i < j \\ \mathbf{G}_{ij} &= \mathbf{G}_{ii} \mathbf{c}_{i-1}^L \mathbf{c}_{i-2}^L \dots \mathbf{c}_j^R & \text{for } i > j.\end{aligned}\quad (18)$$

Depending on the choice of blocks for a given system, these matrix elements may be used to obtain the desired observable.

To apply a solver for tridiagonal matrices to arbitrary systems, a reduction of fairly arbitrary geometries into blocks shown schematically in Fig. 5 must be defined. This is in principle a difficult task, closely related to the graph partitioning problem. Thus a simple and versatile graph partitioning method was defined. Though non-optimal, the simplicity of the algorithm makes it suitable for the application to any lattice geometry.

- Define a starting set of system sites \mathcal{S}_0 . For a transmission calculation, this contains the source and drain lead. For a density calculation, only the source lead sites are included (source and drain leads are abstractions for multiple electrodes, where electrons are injected and not injected respectively).
- Given \mathcal{S}_i , define \mathcal{S}_{i+1} as the collection of all sites s , such that some site in \mathcal{S}_i has a nonzero hopping element to s and none in \mathcal{S}_j for $j < i$ do. Formally

$$\begin{aligned}\mathcal{S}_{i+1} &:= \{s \mid \exists g \in \mathcal{S}_i : t(s, g) \neq 0 \\ &\quad \wedge k < i \implies \forall g \in \mathcal{S}_k : t(s, g) = 0\}.\end{aligned}$$

- Stop when $\mathcal{S}_i = \emptyset$.

These \mathcal{S}_i define a natural block structure for any system geometry with reasonably small matrix dimensions producing a block tridiagonal Hamilton matrix. For the

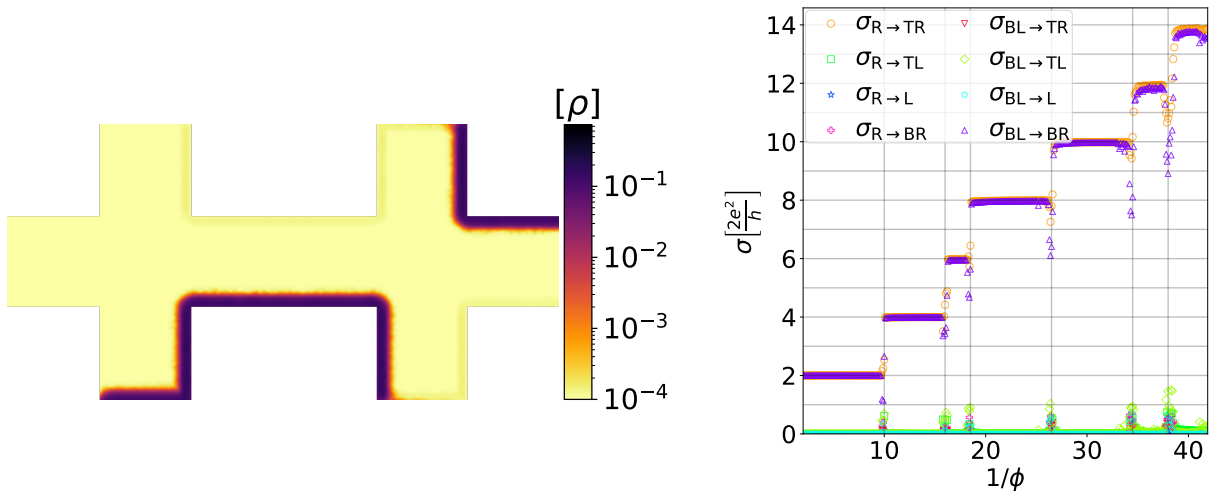


FIG. 6. Hall bar plot for a homogeneous AB stacked Hall bar system. On the left is a logarithmic plot of the LDOS due to electron injection from the lower left and right lead with a cutoff at 1×10^{-4} . On the right are the elements of the conductance tensor. The different conductances have different colors and marker styles. The indices for the conductances are as indicated in Fig. 4. The LDOS calculation is performed at an external magnetic field $\phi_{\text{LDOS}}^{-1} = 10.5\phi_0^{-1}$. The number of sites contained in the system used for the LDOS calculation is $N_L \approx 5 \times 10^5$. The number of sites contained in the system used for the transmission calculation is $N_C \approx 1.5 \times 10^5$.

transmission calculations only the matrix elements contained in \mathcal{S}_0 are calculated and for density calculations matrix elements from \mathcal{S}_0 to all \mathcal{S}_i are calculated. This has the formal difference to [48], that for transmission calculations the source and drain electrodes are considered to both be elements of the first matrix block leading to more favourable block structures for particularly complicated geometries.

The methods described here will all be applied to the Hallbar geometry discussed earlier for which each lead self-energy calculation can be performed separately and for which the system blocking should be similar to the one shown in Fig. 5. In order to perform parameter studies in a reasonable time frame, systems of the order 10^5 sites were chosen implying a maximal matrix block size of $\approx 10^3$. The self-energy calculation without optimization would involve matrices of the order $\approx 4 \times 10^3$, but is reduced to $\approx 10^3$ reducing the runtime considerably due to the cubic complexity of all matrix algorithms involved.

V. RESULTS

In this section we present and discuss our magnetoconductance calculations for the introduced BLG systems. First, results for the the homogeneous system will be described as an important reference. In a next step the hard wall layer switching system is investigated as a very simple model for an LSW. Then the more realistic sheared Hall bar with an LSW along the armchair nanoribbon and the tensile Hall bar with an LSW along the zigzag nanoribbon are studied. For each system an LDOS calculation will be shown. In addition, since the latter only show the properties at a single magnetic field value, conductance

calculations are also shown for more in-depth analysis of system properties with respect to the external magnetic field.

A. Homogeneous bilayer graphene system

As a reference and in order to check the validity of our numerical implementation, we first discuss a homogeneous AB stacked BLG system with a Hall bar geometry. The LDOS and conductance calculations for the homogeneous system are displayed in Fig. 6. Both the LDOS and conductance calculation indeed show the expected behaviour for a homogeneous BLG system. The LDOS calculation in Fig. 6 clearly displays modes for a magnetic field $\phi_{\text{LDOS}}^{-1} = 10.5\phi_0^{-1}$ located within the second conductance plateau, that are localized at the system edge. The propagation direction due to the magnetic field defined in Fig. 4 is also in agreement with the expected anti-clockwise cyclotron orbits.

The conductance calculation displayed on the right of Fig. 6 already has a lot of structure, even for the homogeneous system. Since spin is not accounted for, the plateau structure is $2(n+1)$ for $n = 0, 1, 2, \dots$ affirming an anomalous integer quantum Hall effect due to the degeneracy of the first Landau level. The weakening of the localization argument at the edges of the Landau levels can also be clearly seen in the nonzero contributions to the conductance e.g. in $\sigma_{\text{BL} \rightarrow \text{TL}}$, which would be characterized by nonzero LDOS inside the material bulk implying the contribution of previously gapped bulk states. Another striking aspect of the conductance plateau is their irregular spacing caused by the underlying electronic structure of BLG, that modifies the equidistant

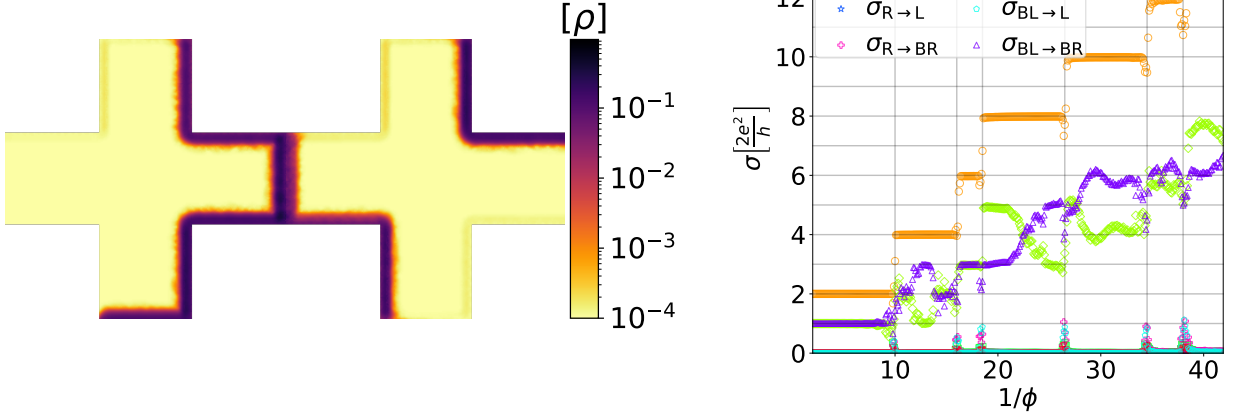


FIG. 7. Hall bar plot, see Fig. 6, for a Hall bar system with HLSW. The LDOS calculation is performed at an external magnetic field $\phi_{\text{LDOS}}^{-1} = 10.5\phi_0^{-1}$. The lower layer is fully coupled $t_{\text{LSW}}^{(1)} = t$. The upper layer is decoupled $t_{\text{LSW}}^{(2)} = 0$. The number of sites contained in the system used for the LDOS calculation is $N_L \approx 5 \times 10^5$. The number of sites contained in the system used for the transmission calculation is $N_C \approx 1.5 \times 10^5$.

free (purely parabolic dispersion) electron solution [27]. At larger values of $1/\phi$ (smaller magnetic fields), in particular for the sixth plateau, the larger magnetic length scale implied by the external magnetic field already leads to some finite-size effects, causing the occupation of bulk modes which do not appear in a macroscopically large material. This is particularly obvious, when comparing $\sigma_{R \rightarrow TR}$ for which the gauge was chosen to be commensurate with the injection lead periodicity and $\sigma_{BL \rightarrow BR}$ for which the gauge was thus not compatible with the injection lead periodicity, such that localization of bulk modes in the smaller material section in the bottom left fails for higher Landau levels.

B. Hard wall layer switching system

Representative results for the HLSW model as illustrated in Fig. 2 with a decoupled upper layer and a fully coupled lower layer are displayed in Fig. 7. The conductance curves of particular interest are $\sigma_{BL \rightarrow BR}$, which corresponds to the conductance across the LSW, and $\sigma_{BL \rightarrow TL}$, which corresponds to the conductance parallel to the LSW. As long as the transport states are localized at the system edge, implying little finite-size effects and a magnetic field value not located at a plateau edge, $\sigma_{R \rightarrow TR}$ is a reference to the integer quantum Hall conductance in a homogeneous BLG sample as discussed in the last subsection. Indeed, as expected, the conductance $\sigma_{R \rightarrow TR}$ far away from the HLSW is the same as the one for the homogeneous system in Fig. 6, exhibiting a typical anomalous IQHE in BLG.

The LDOS calculation in Fig. 7 shows localized edge modes just as in Fig. 6 when far away from the HLSW. There is however also an increase in electron density in the region of the HLSW, indicating transport parallel to

the HLSW from the electrode *BL* towards the electrode *TL*. The quantities $\sigma_{BL \rightarrow TL}$ and $\sigma_{R \rightarrow TR}$ most related to the structure of the LSW have an entirely different structure from the homogeneous BLG system. First of all, $\sigma_{BL \rightarrow BR} + \sigma_{BL \rightarrow TL} = \sigma_{R \rightarrow TR}$ for all values of ϕ^{-1} not close to plateau transitions in $\sigma_{R \rightarrow TR}$. This strengthens the intuition, that the TLSW either causes conductance parallel or transverse to it and no scattering to any other electrode occurs when the edge modes are sufficiently localized in the homogeneous system.

For large magnetic fields (small ϕ^{-1}), the homogeneous system exhibits a conductance of $\sigma_{BL \rightarrow BR} = 2\sigma_o$, whereas the decoupled HLSW system has the value $\sigma_{BL \rightarrow BR} = \sigma_o$. This reflects the fact, that only the lower layer is coupled and the mode localized at the edge of the upper layer thus propagates parallel to the HLSW, which acts as a system edge of the upper sheet. This can also be confirmed by closer examination of an LDOS calculation for large magnetic fields (not shown). With a similar intuition, the magnitude of $\sigma_{BL \rightarrow BR}$ and $\sigma_{BL \rightarrow TL}$ seems to be similar when averaged over an entire plateau. $\sigma_{BL \rightarrow TL}$ is larger at the edges of plateaus and $\sigma_{BL \rightarrow BR}$ at the centers. Physically, an explanation similar to the reasoning for the existence of larger longitudinal conductance at plateau transitions is reasonable corresponding to available delocalized modes to scatter into.

A study of the full parameter dependence on $t_{\text{LSW}}^{(U)} \in [0, t]$ is shown in Fig. 8. Only $\sigma_{BL \rightarrow BR}$ and $\sigma_{BL \rightarrow TL}$ are shown, since the behaviour of the other conductance are essentially the same as for the homogeneous system for all parameter values. The limiting cases $t_{\text{LSW}}^{(U)} = 0$ and $t_{\text{LSW}}^{(U)} = t$ have no special properties. As expected, $\sigma_{BL \rightarrow BR}$ is larger for larger $t_{\text{LSW}}^{(U)}$ and $\sigma_{BL \rightarrow TL}$ is smaller. There is no formation of a plateau structure in $\sigma_{BL \rightarrow BR}$ or $\sigma_{BL \rightarrow TL}$ for any value of $t_{\text{LSW}}^{(U)}$.

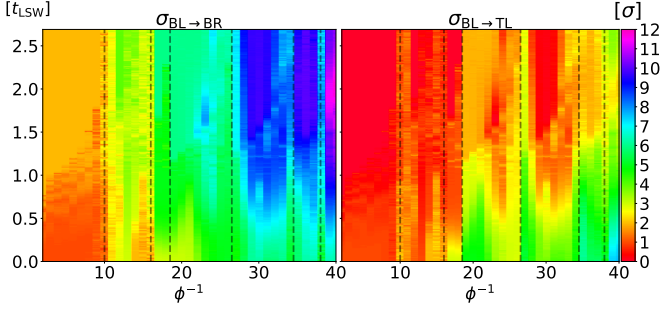


FIG. 8. Parameter study of the HLSW interaction strength $t_{\text{LSW}}^{(U)}$ for different external magnetic fields ϕ^{-1} for a HLSW system. On the left is $\sigma_{\text{BL} \rightarrow \text{BR}}$ and on the right is $\sigma_{\text{BL} \rightarrow \text{TL}}$. The two plots show the conductance in color with the HLSW interaction strength $t_{\text{LSW}}^{(U)}$ on the y-axis and the magnetic field on the x-axis. The number of sites in the system used for the transmission calculations is $N_C \approx 1.6 \times 10^5$.

The tendency of a larger magnitude in $\sigma_{\text{BL} \rightarrow \text{BR}}$ close to the centers of plateaus persists for all $t_{\text{LSW}}^{(U)} \in [0, t]$.

C. Sheared layer switching system

Next we turn to our findings for a more realistic model of an LSW, which is formed due to shear in the upper graphene layer as illustrated in Fig. 3. Representative results are shown in Fig. 9. Just as for the HLSW system in Fig. 7, the LDOS calculation shows localized edge modes away from the SLSW and an increased density in the region of the SLSW itself. The region of increased density however is larger than the region for the HLSW system in Fig. 7. This is due to the finite extent of the LSW, which allows for propagation parallel to the LSW over the whole range of the LSW.

The particular choice of $L_s = 44$ in Fig. 9 is such that the system is neither in the limit of a very small nor a very large SLSW. The corresponding conductance calculations in Fig. 9 confirm that there is conductance parallel to the SLSW. Both conductance functions $\sigma_{\text{BL} \rightarrow \text{BR}}$ and $\sigma_{\text{BL} \rightarrow \text{TL}}$ are almost monotonous and form approximate plateaus, albeit not for the same ϕ -range as $\sigma_{\text{R} \rightarrow \text{TR}}$. In particular around the center of the plateaus, the conductances $\sigma_{\text{BL} \rightarrow \text{BR}}$ and $\sigma_{\text{BL} \rightarrow \text{TL}}$ are almost constant.

A parameter study of the shear strength parameter L_s is displayed in Fig. 10. There is a well defined limit of the conductances $\sigma_{\text{BL} \rightarrow \text{BR}}$ and $\sigma_{\text{BL} \rightarrow \text{TL}}$ for $L_s \rightarrow \infty$, which is reached in the interval $\phi^{-1} \in [0, 40]$ for any values $L_s > 100$. The convergence clearly depends on the value of the external magnetic field. This is reasonable, since a larger value of ϕ^{-1} implies a larger magnetic length $l_B = \sqrt{\frac{\hbar c}{eB}}$. Thus the limit $L_s \rightarrow \infty$ is reached for larger L_s when ϕ^{-1} is chosen larger. The resolution of the conductances along the magnetic field axis is however not good enough to confirm a quadratic dependence on L_s , which would be expected. It is clear that $\sigma_{\text{BL} \rightarrow \text{TL}}$ being al-

most monotonous for $L_s = 44$ in Fig. 9 is no longer true for the infinitely smooth shear transition $L_s \rightarrow \infty$. However, both $\sigma_{\text{BL} \rightarrow \text{TL}}$ and $\sigma_{\text{BL} \rightarrow \text{BR}}$ exhibit a plateau structure in the limit $L_s \rightarrow \infty$. Further, the limit for $\sigma_{\text{BL} \rightarrow \text{BR}}$ is a monotonous plateau structure. The non-converged values in the small shear width limit are generically smaller than the values in the opposite limit of large shear widths. This is reasonable, if the SLSW were to be modeled by some potential wall that is thicker for a wider SLSW.

The limiting case $L_s \rightarrow \infty$ is investigated in Fig. 11 for the choice $L_s = 150$. The monotonous plateau structure of $\sigma_{\text{BL} \rightarrow \text{BR}}$ mentioned in the discussion of Fig. 10 is now readily apparent. It is also confirmed, that $\sigma_{\text{BL} \rightarrow \text{TL}}$ exhibits a non-monotonous plateau structure since the plateaus of $\sigma_{\text{BL} \rightarrow \text{BR}}$ and $\sigma_{\text{R} \rightarrow \text{TR}}$ are not aligned and $\sigma_{\text{BL} \rightarrow \text{BR}} + \sigma_{\text{BL} \rightarrow \text{TL}} = \sigma_{\text{R} \rightarrow \text{TR}}$. The plateau structure of $\sigma_{\text{BL} \rightarrow \text{BR}}$ is:

- $\phi^{-1} \in [0, 21] \Rightarrow \sigma_{\text{BL} \rightarrow \text{BR}} = 2\sigma_0$.
- $\phi^{-1} \in [21, 32] \Rightarrow \sigma_{\text{BL} \rightarrow \text{BR}} = 4\sigma_0$.
- $\phi^{-1} \in [32, 40] \Rightarrow \sigma_{\text{BL} \rightarrow \text{BR}} = 6\sigma_0$.

D. Tensile layer switching system

Representative results for a system where the LSW is formed due to tension, see Fig. 3, are shown in Fig. 12. Just as for the SLSW system the choice of $L_t = 60$ is an intermediate value, neither in the $L_t \rightarrow 0$ nor the $L_t \rightarrow \infty$ limit. The LDOS calculation yields similar results as calculations for the HLSW and SLSW systems, an increased density near edges away from the TLSW and an increased density in the region of the TLSW. The density increase in the region of the TLSW is however much more extended than for the cases of the SLSW and the HLSW. This is due to the fact, that the choice of LSW here is wider than in any of the other systems. Note that a similar distribution of the electron density may be also observed for systems of the SLSW type with wider LSW. Thus, although the LDOS in the transition regime of the LSW is the largest, there are also relevant contributions in its interior.

$\sigma_{\text{R} \rightarrow \text{TR}}$ is once again not affected by the presence of an LSW. The conductance functions $\sigma_{\text{BL} \rightarrow \text{TL}}$ and $\sigma_{\text{BL} \rightarrow \text{BR}}$ in Fig. 12 are not as simple as in Fig. 7 or Fig. 9 due to the TLSW geometry. The conductances, in particular $\sigma_{\text{BL} \rightarrow \text{BR}}$, clearly have regions where they are approximately constant. This indicates a tendency for a plateau formation, but there are still relevant fluctuations of the order σ_0 in regions of almost constant conductance. These areas of plateau formation are also interrupted by plateau transitions in $\sigma_{\text{R} \rightarrow \text{TR}}$, but this is to be expected with a similar explanation as for the SLSW and HLSW systems.

Since the plateau formation might be more obvious in the limit $L_t \rightarrow \infty$ as for the SLSW system, a parameter study of the TLSW system with respect to L_t is shown in Fig. 13. However, the fluctuations seen in Fig. 12

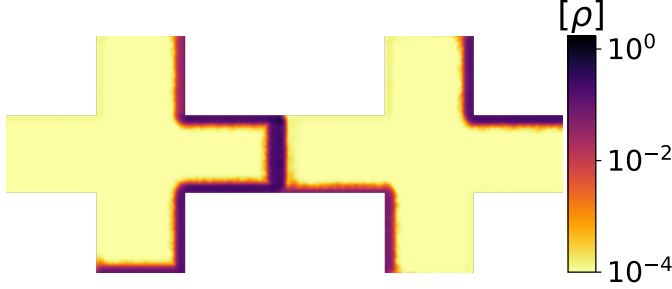


FIG. 9. Hall bar plot, see Fig. 6, for a Hall bar system with SLSW. The LDOS calculation is performed at an external magnetic field $\phi_{\text{LDOS}}^{-1} = 10.5\phi_0^{-1}$. The cutoff between the two layers in the LSW is long, $D_C = 4a_0$. The shear width parameter is $L_S = 44$. The number of sites contained in the system used for the LDOS calculation is $N_L \approx 1.2 \times 10^6$. The number of sites contained in the system used for the transmission calculation is $N_C \approx 2.3 \times 10^5$.

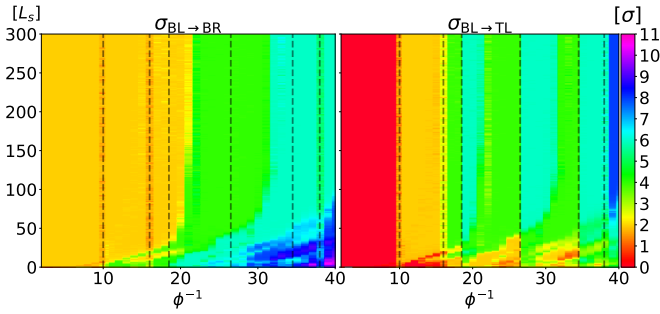


FIG. 10. Parameter study of the SLSW width L_s for different external magnetic fields ϕ^{-1} for a SLSW system. On the left is $\sigma_{\text{BL} \rightarrow \text{BR}}$ and on the right is $\sigma_{\text{BL} \rightarrow \text{TL}}$. The two plots show the conductance in color with the SLSW width L_s on the y-axis and the magnetic field on the x-axis. The number of sites in the system used for the transmission calculations is $N_C \approx 2.3 \times 10^5$. The cutoff between the two layers in the LSW is long, $D_C = 4a_0$.

are persistent for all studied values of L_t , including the $L_t \rightarrow \infty$ limit. There is a fixed limit $L_t \rightarrow \infty$ up to persistent fluctuations. Our conclusion to the persistence of the fluctuations is that the TLSW system simply reacts more strongly to small changes in external parameters than the SLSW or HLSW systems. This is also confirmed by further discussions in Appendices A and B. When examining the whole range of L_t it becomes apparent, that the $L_t \rightarrow \infty$ limit exhibits a very similar plateau formation as the $L_s \rightarrow \infty$ limit for the SLSW system, but with fluctuations of order σ_0 . This means, there is a monotonous plateau structure in $\sigma_{\text{BL} \rightarrow \text{BR}}$ and a non-monotonous plateau structure in $\sigma_{\text{BL} \rightarrow \text{TL}}$. Similar to the SLSW system, the convergence with respect to system size is faster for smaller ϕ^{-1} and the magnitude of $\sigma_{\text{BL} \rightarrow \text{BR}}$ is smaller for smaller L_t . The physical interpretations for these phenomena are therefore the same as the SLSW

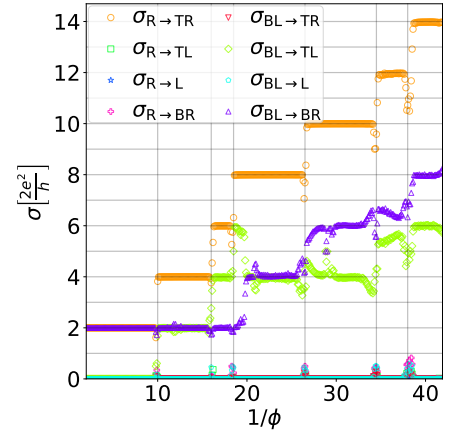


FIG. 11. Transmission calculation like in **Hall bar plot**, see Fig. 6, for a Hall bar system with SLSW. The cutoff between the two layers in the LSW is long, $D_C = 4a_0$. The shear width parameter is $L_S = 150$. For both calculations The number of sites contained in the system used for the transmission calculation is $N_C \approx 2.3 \times 10^5$.

system.

As an example for the $L_t \rightarrow \infty$ limit, a TLSW system with $L_t = 150$ is shown in Fig. 14. When examining a single magnetoconductance slice of the L_t parameter study, the plateau formation is not as obvious. In the context of Fig. 13, we can identify the regions of almost constant conductance. Close to the plateau centers of $\sigma_{\text{R} \rightarrow \text{TR}}$, the following implications hold:

- $\phi^{-1} \in [2, 10] \Rightarrow \sigma_{\text{BL} \rightarrow \text{BR}} \in [\sigma_0, 2\sigma_0]$.
- $\phi^{-1} \in [10, 21] \Rightarrow \sigma_{\text{BL} \rightarrow \text{BR}} \in [2\sigma_0, 3\sigma_0]$.
- $\phi^{-1} \in [21, 32] \Rightarrow \sigma_{\text{BL} \rightarrow \text{BR}} \in [4\sigma_0, 5\sigma_0]$.

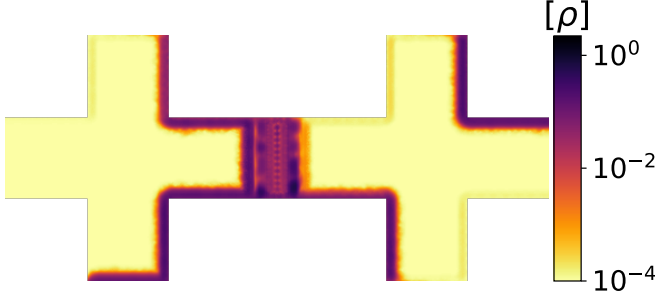


FIG. 12. Hall bar plot, see Fig. 6, for a tensed system. The LDOS calculation is performed at an external magnetic field $\phi_{\text{LDOS}}^{-1} = 10.5\phi_0^{-1}$. The cutoff between the two layers in the LSW is short, $D_C = 1.3a_0$. The tension length parameter is $L_T = 60$. The number of sites contained in the system used for the LDOS calculation is $N_L \approx 8.1 \times 10^5$. The number of sites contained in the system used for the transmission calculation is $N_C \approx 2.0 \times 10^5$.

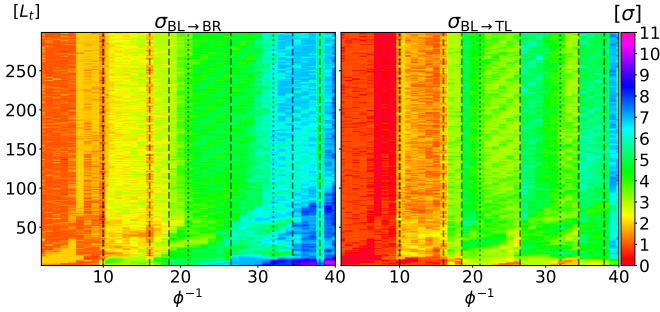


FIG. 13. Parameter study of the TLSW width L_t for different external magnetic fields ϕ^{-1} for a TLSW system. On the left is $\sigma_{\text{BL} \rightarrow \text{BR}}$ and on the right is $\sigma_{\text{BL} \rightarrow \text{TL}}$. The two plots show the conductance in color with the TLSW width L_t on the y-axis and the magnetic field on the x-axis. The number of sites in the system used for the transmission calculations is $N_C \approx 2.0 \times 10^5$. The cutoff between the two layers in the LSW is long, $D_C = 4a_0$.

- $\phi^{-1} \in [32, 40] \Rightarrow \sigma_{\text{BL} \rightarrow \text{BR}} \in [5\sigma_0, 6\sigma_0]$.

These plateau definitions are consistent with Fig. 13.

VI. CONCLUSIONS

We have investigated the effects of different LSWs in BLG in the IQHE regime on the conductance and the LDOS given a Hall bar geometry. The particular types of LSWs investigated were a hard wall LSW parallel to the zigzag nanoribbon, a shear LSW parallel to the armchair nanoribbon, and a tensile LSW parallel to the zigzag nanoribbon. Additionally, the homogeneous BLG system was discussed as a reference and to establish the basic properties of AB stacked BLG in the IQHE regime.

Aside from the investigation of the different BLG systems we have expanded upon the usual methods employed

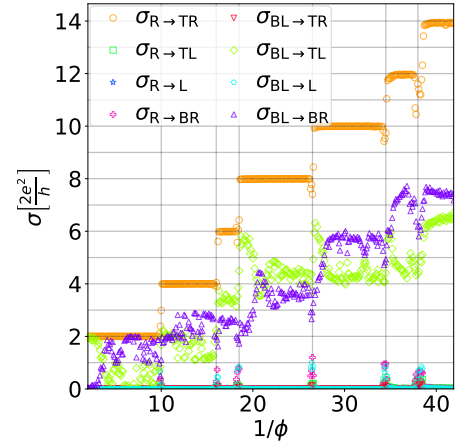


FIG. 14. Transmission calculation like in **Hall bar plot**, see Fig. 6, for a tensed Hall bar system. The cutoff between the two layers in the LSW is long, $D_C = 4a_0$. The tension length parameter is $L_T = 150$. For both calculations The number of sites contained in the system used for the transmission calculation is $N_C \approx 2.0 \times 10^5$.

in the calculation of such transport properties. For the calculation of the self energy due to a semi-infinite lead, an optimization for sparse chain couplings with a significant dimensional reduction was introduced. To perform the simulation of transport properties in a Hall bar geometry a general and stable scheme for the partition of a BLG lattice on arbitrary geometries was formulated. Although this solution is not optimal for all geometries, the performance in all applications presented in this paper was satisfactory.

The results for the homogeneous BLG without LSWs were as expected, with all features in the LDOS and conductance accounted for like the sequence of non-equidistant conductance plateaus with the expected sequence of conductance quantum multiples and the appro-

appropriate edge localization of the corresponding modes. We found that the hard wall system behaves significantly different from the tensile and shear systems. It is therefore not a particularly good model for any choice of hopping elements. Further, there are no obvious limiting cases for $t_{\text{LSW}}^{(U)} = 0$ or $t_{\text{LSW}}^{(U)} = t$. In contrast, the tensile system shows persistent fluctuations of order σ_0 in $\sigma_{\text{BL} \rightarrow \text{BR}}$ and $\sigma_{\text{BL} \rightarrow \text{TL}}$ even for large values of L_t . Both the tensile and the shear system have indeed a well defined limit $L_{s/t} \rightarrow \infty$ (up to fluctuations in case of the tensile system). Convergence for both limits L_s and L_t depends on the external magnetic field where larger ϕ^{-1} imply slower convergence. Most importantly, both limits $L_s \rightarrow \infty$ and $L_t \rightarrow \infty$ show monotonous plateau structure in $\sigma_{\text{BL} \rightarrow \text{BR}}$ and non-monotonous plateau structure in $\sigma_{\text{BL} \rightarrow \text{TL}}$. The values of these plateaus are always integer multiples of the elementary conductance quantum σ_0 .

One motivation for our study was the perceived ambiguity between fractionalization due to geometry and due to electron-electron interaction effects. For all types of LSWs investigated, conductance plateaus that do not appear for the ordinary IQHE can certainly be achieved simply due to geometrical effects and the effect of multiple LSW geometries on the conductance is still unclear from the results presented here. What can be said is that the effect of LSWs is highly nontrivial and very geometry-dependant. Thus, it certainly requires a fully quantum mechanical description in general.

There are several additional issues, for which further investigations would be desirable. The most obvious one stems from the motivation of the research and is the calculation of conductance functions and densities for systems

with multiple LSWs and ultimately to model entire defect networks like in real materials. In particular, a potential fractionalization of the conductance for multiple LSWs in different geometrical configurations would be very interesting. With more computing time larger systems and thus a larger range of magnetic field values could be reliably studied even in a full parameter study. Another aspect, that has not been fully investigated is the different system geometries that are possible. On one hand the proper modeling of buckling would extend the discussion to more experimentally available systems. On the other hand, the hard wall model parallel to the armchair nanoribbon should at least be investigated for completeness. Another LSW geometry, that has not been investigated in our work is an LSW due to a change of interaction cutoff as discussed in the appendix to differentiate between effects due to the choice of a different value in the LSW region and effects of the actual LSW geometry. Since the LSWs due to shear and tension show some similarities to twisted bilayer graphene, for which interactions are indeed important for small twist angles, electron-electron interactions might also be relevant and should thus be modeled for the tensile and shear LSW models. For a microscopic lattice model this is computationally not feasible for reasonably large systems. Thus, a different approach to the system modeling or some simplification to the interaction would have to be employed.

VII. ACKNOWLEDGMENTS

We thank Sam Shallcross and Heiko Weber for fruitful discussions.

-
- ¹ F. Bonaccorso, A. Lombardo, T. Hasan, Z. Sun, L. Colombo, and A. C. Ferrari, *Materials Today* **15**, 564 (2012).
 - ² A. K. Geim and I. V. Grigorieva, *Nature* **499**, 419 (2013).
 - ³ X.-L. Qi and S.-C. Zhang, *Rev. Mod. Phys.* **83**, 1057 (2011).
 - ⁴ M. Z. Hasan and C. L. Kane, *Rev. Mod. Phys.* **82**, 3045 (2010).
 - ⁵ A. P. Schnyder, S. Ryu, A. Furusaki, A. W. W. Ludwig, V. Lebedev, and M. Feigelman, *AIP Conference Proceedings* **1134**, 10 (2009), <https://aip.scitation.org/doi/pdf/10.1063/1.3149481>.
 - ⁶ A. Y. Kitaev, *Physics-Uspekhi* **44**, 131 (2001).
 - ⁷ A. Kitaev, V. Lebedev, and M. Feigelman, *AIP Conference Proceedings* **1134**, 22 (2009), <https://aip.scitation.org/doi/pdf/10.1063/1.3149495>.
 - ⁸ A. Kitaev, *Annals of Physics* **303**, 2 (2003).
 - ⁹ M. H. Freedman, A. Kitaev, M. J. Larsen, and Z. Wang (2003) pp. 31–38, *mathematical challenges of the 21st century* (Los Angeles, CA, 2000).
 - ¹⁰ R. B. Laughlin, *Phys. Rev. Lett.* **50**, 1395 (1983).
 - ¹¹ D. C. Tsui, H. L. Stormer, and A. C. Gossard, *Phys. Rev. Lett.* **48**, 1559 (1982).
 - ¹² L. Balents, *Nature* **464**, 199 (2010).
 - ¹³ C. L. Kane and E. J. Mele, *Phys. Rev. Lett.* **95**, 226801 (2005).
 - ¹⁴ I. W. Frank, D. M. Tanenbaum, A. M. van der Zande, and P. L. McEuen, *Journal of Vacuum Science & Technology B: Microelectronics and Nanometer Structures Processing, Measurement, and Phenomena* **25**, 2558 (2007), <https://avs.scitation.org/doi/pdf/10.1116/1.2789446>.
 - ¹⁵ F. Schwierz, *Nature Nanotechnology* **5**, 487 (2010).
 - ¹⁶ *Nature Nanotechnology* **4**, 839 (2009).
 - ¹⁷ T. Ohta, A. Bostwick, T. Seyller, K. Horn, and E. Rotenberg, *Science* **313**, 951 (2006), <https://science.sciencemag.org/content/313/5789/951.full.pdf>.
 - ¹⁸ Y. Zhang, T.-T. Tang, C. Girit, Z. Hao, M. C. Martin, A. Zettl, M. F. Crommie, Y. R. Shen, and F. Wang, *Nature* **459**, 820 (2009).
 - ¹⁹ E. McCann and M. Koshino, *Reports on Progress in Physics* **76**, 056503 (2013).
 - ²⁰ E. Suárez Morell, J. D. Correa, P. Vargas, M. Pacheco, and Z. Barticevic, *Phys. Rev. B* **82**, 121407 (2010).
 - ²¹ S. Huang, K. Kim, D. K. Efimkin, T. Lovorn, T. Taniguchi, K. Watanabe, A. H. MacDonald, E. Tutuc, and B. J. LeRoy, *Phys. Rev. Lett.* **121**, 037702 (2018).
 - ²² M. Yankowitz, S. Chen, H. Polshyn, Y. Zhang, K. Watanabe, T. Taniguchi, D. Graf, A. F. Young, and C. R. Dean, *Science* **363**, 1059 (2019),

- <https://science.sciencemag.org/content/363/6431/1059.full.pdf>
- ²³ Y. Cao, V. Fatemi, A. Demir, S. Fang, S. L. Tomarken, J. Y. Luo, J. D. Sanchez-Yamagishi, K. Watanabe, T. Taniguchi, E. Kaxiras, R. C. Ashoori, and P. Jarillo-Herrero, *Nature* **556**, 80 (2018).
 - ²⁴ Y. Cao, V. Fatemi, S. Fang, K. Watanabe, T. Taniguchi, E. Kaxiras, and P. Jarillo-Herrero, *Nature* **556**, 43 (2018).
 - ²⁵ A. H. Castro Neto, F. Guinea, N. M. R. Peres, K. S. Novoselov, and A. K. Geim, *Rev. Mod. Phys.* **81**, 109 (2009).
 - ²⁶ V. P. Gusynin and S. G. Sharapov, *Phys. Rev. Lett.* **95**, 146801 (2005).
 - ²⁷ K. S. Novoselov, E. McCann, S. V. Morozov, V. I. Fal'ko, M. I. Katsnelson, U. Zeitler, D. Jiang, F. Schedin, and A. K. Geim, *Nature Physics* **2**, 177 (2006).
 - ²⁸ K. Yan, H. Peng, Y. Zhou, H. Li, and Z. Liu, *Nano Letters* **11**, 1106 (2011), pMID: 21322597.
 - ²⁹ C. Riedl, C. Coletti, T. Iwasaki, A. A. Zakharov, and U. Starke, *Phys. Rev. Lett.* **103**, 246804 (2009).
 - ³⁰ F. Speck, M. Ostler, J. Röhl, J. Jobst, D. Waldmann, M. Hundhausen, L. Ley, H. B. Weber, and T. Seyller, in *Silicon Carbide and Related Materials 2009*, Materials Science Forum, Vol. 645 (Trans Tech Publications Ltd, 2010) pp. 629–632.
 - ³¹ J. S. Alden, A. W. Tsen, P. Y. Huang, R. Hovden, L. Brown, J. Park, D. A. Muller, and P. L. McEuen, *Proceedings of the National Academy of Sciences* **110**, 11256 (2013), <https://www.pnas.org/content/110/28/11256.full.pdf>.
 - ³² B. Butz, C. Dolle, F. Niekel, K. Weber, D. Waldmann, H. B. Weber, B. Meyer, and E. Spiecker, *Nature* **505**, 533 (2014).
 - ³³ X. Gong and E. J. Mele, *Phys. Rev. B* **89**, 121415 (2014).
 - ³⁴ J. Li, K. Wang, K. J. McFaul, Z. Zern, Y. Ren, K. Watanabe, T. Taniguchi, Z. Qiao, and J. Zhu, *Nature Nanotechnology* **11**, 1060 (2016).
 - ³⁵ L. Ju, Z. Shi, N. Nair, Y. Lv, C. Jin, J. Velasco, C. Ojeda-Aristizabal, H. A. Bechtel, M. C. Martin, A. Zettl, J. Analytis, and F. Wang, *Nature* **520**, 650 (2015).
 - ³⁶ P. Rickhaus, J. Wallbank, S. Slizovskiy, R. Pisoni, H. Overweg, Y. Lee, M. Eich, M.-H. Liu, K. Watanabe, T. Taniguchi, T. Ihn, and K. Ensslin, *Nano Letters* **18**, 6725 (2018).
 - ³⁷ L.-J. Yin, H. Jiang, J.-B. Qiao, and L. He, *Nature Communications* **7**, 11760 (2016).
 - ³⁸ F. Kisslinger, C. Ott, C. Heide, E. Kampert, B. Butz, E. Spiecker, S. Shallcross, and H. B. Weber, *Nature Physics* **11**, 650 (2015).
 - ³⁹ P. San-Jose, R. V. Gorbachev, A. K. Geim, K. S. Novoselov, and F. Guinea, *Nano Letters* **14**, 2052 (2014), pMID: 24605877, <https://doi.org/10.1021/nl500230a>.
 - ⁴⁰ S. Shallcross, S. Sharma, and H. B. Weber, *Nature Communications* **8**, 342 (2017).
 - ⁴¹ D. Weckbecker, R. Gupta, F. Rost, S. Sharma, and S. Shallcross, *Phys. Rev. B* **99**, 195405 (2019).
 - ⁴² P. Maher, L. Wang, Y. Gao, C. Forsythe, T. Taniguchi, K. Watanabe, D. Abanin, Z. Papić, P. Cadden-Zimansky, J. Hone, P. Kim, and C. R. Dean, *Science* **345**, 61 (2014), <https://science.sciencemag.org/content/345/6192/61.full.pdf>.
 - ⁴³ A. Kou, B. E. Feldman, A. J. Levin, B. I. Halperin, K. Watanabe, T. Taniguchi, and A. Yacoby, *Science* **345**, 55 (2014).
 - ⁴⁴ Y. Barlas, R. Côté, K. Nomura, and A. H. MacDonald, *Phys. Rev. Lett.* **101**, 097601 (2008).
 - ⁴⁵ F. Kisslinger, D. Rienmüller, C. Ott, E. Kampert, and H. B. Weber, *Annalen der Physik* **531**, 1800188 (2019).
 - ⁴⁶ D. J. Thouless and S. Kirkpatrick, *Journal of Physics C: Solid State Physics* **14**, 235 (1981).
 - ⁴⁷ C. H. Lewenkopf and E. R. Mucciolo, *Journal of Computational Electronics* **12**, 203 (2013).
 - ⁴⁸ D. E. Petersen, H. H. B. Sørensen, P. C. Hansen, S. Skelboe, and K. Stokbro, *Journal of Computational Physics* **227**, 3174 (2008).
 - ⁴⁹ P. A. Khomyakov and G. Brocks, *Phys. Rev. B* **70**, 195402 (2004).
 - ⁵⁰ P. A. Khomyakov, G. Brocks, V. Karpan, M. Zwierzycki, and P. J. Kelly, *Phys. Rev. B* **72**, 035450 (2005).
 - ⁵¹ J. Rammer and H. Smith, *Rev. Mod. Phys.* **58**, 323 (1986).
 - ⁵² A. Cresti, R. Farchioni, G. Grosso, and G. P. Parravicini, *Phys. Rev. B* **68**, 075306 (2003).
 - ⁵³ P. Moon and M. Koshino, *Phys. Rev. B* **85**, 195458 (2012).
 - ⁵⁴ F. Zhang, A. H. MacDonald, and E. J. Mele, *Proceedings of the National Academy of Sciences* **110**, 10546 (2013), <https://www.pnas.org/content/110/26/10546.full.pdf>.
 - ⁵⁵ C. W. Groth, M. Wimmer, A. R. Akhmerov, and X. Waintal, *New Journal of Physics* **16**, 063065 (2014).
 - ⁵⁶ K. Kazymyrenko and X. Waintal, *Phys. Rev. B* **77**, 115119 (2008).
 - ⁵⁷ D. H. Lee and J. D. Joannopoulos, *Phys. Rev. B* **23**, 4997 (1981).
 - ⁵⁸ T. Ando, *Phys. Rev. B* **44**, 8017 (1991).
 - ⁵⁹ H. H. B. Sørensen, P. C. Hansen, D. E. Petersen, S. Skelboe, and K. Stokbro, *Phys. Rev. B* **77**, 155301 (2008).
 - ⁶⁰ M. P. L. Sancho, J. M. L. Sancho, J. M. L. Sancho, and J. Rubio, *Journal of Physics F: Metal Physics* **15**, 851 (1985).

Appendix A: Finite-size effects

The magnitude of finite-size effects is magnetic field dependent and it is of great importance to check the previous calculations for convergence with respect to system size. We will discuss three system sizes for HLSW with decoupled upper sheet, SLSW and TLSW each.

1. Hard wall layer switching system

A finite-size study for HLSW systems with decoupled upper layer is shown in Fig. 15. Comparing Fig. 15a, Fig. 15b and Fig. 15c, it is clear that there are some finite-size effects in the calculations of smaller systems. Particularly for the transmissions $\sigma_{BL \rightarrow BR}$ and $\sigma_{BL \rightarrow TL}$ in the regime of smaller magnetic field (the last three plateaus), features are still changing with system size. Increases and decreases in the conductivity are sharper for larger system sizes in this region. For smaller plateaus however, the system has already converged to a satisfactory degree for the smallest system size. The general shape of the conductivities does also not change with system size.

2. Sheared layer switching system

A finite-size study for SLSW systems is shown in Fig. 16. The conductance functions for all three system sizes are almost identical, particularly for the first four plateaus.

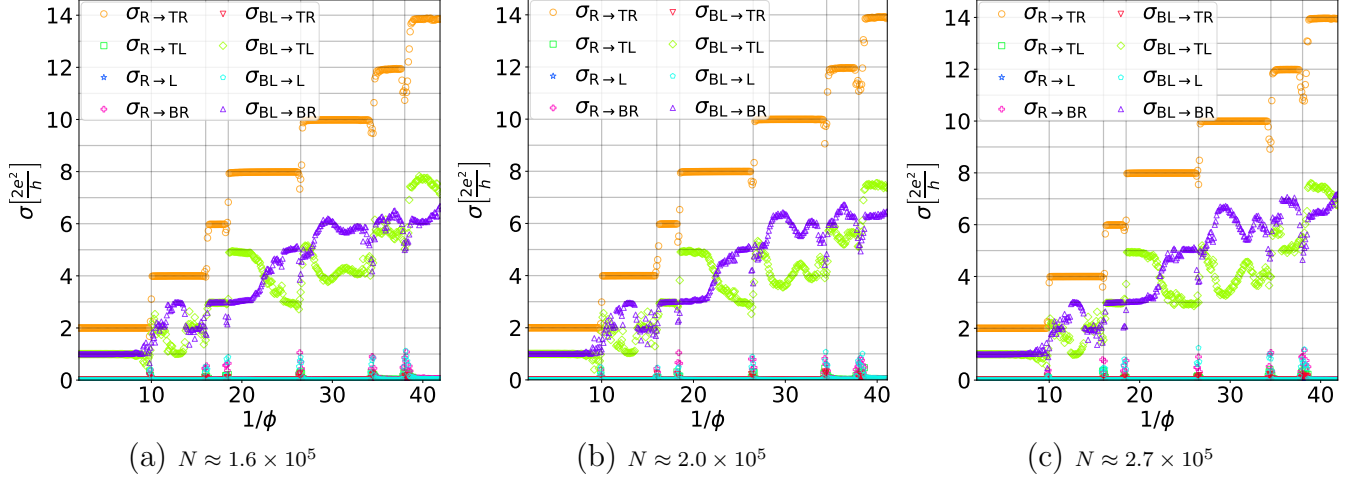


FIG. 15. HLSW Hall bar system finite-size analysis for transmission diagrams, see Fig. 6 for a description of transmission diagrams. The lower layer is fully coupled $t_{\text{LSW}}^{(1)} = t$. The upper layer is decoupled $t_{\text{LSW}}^{(2)} = 0$.

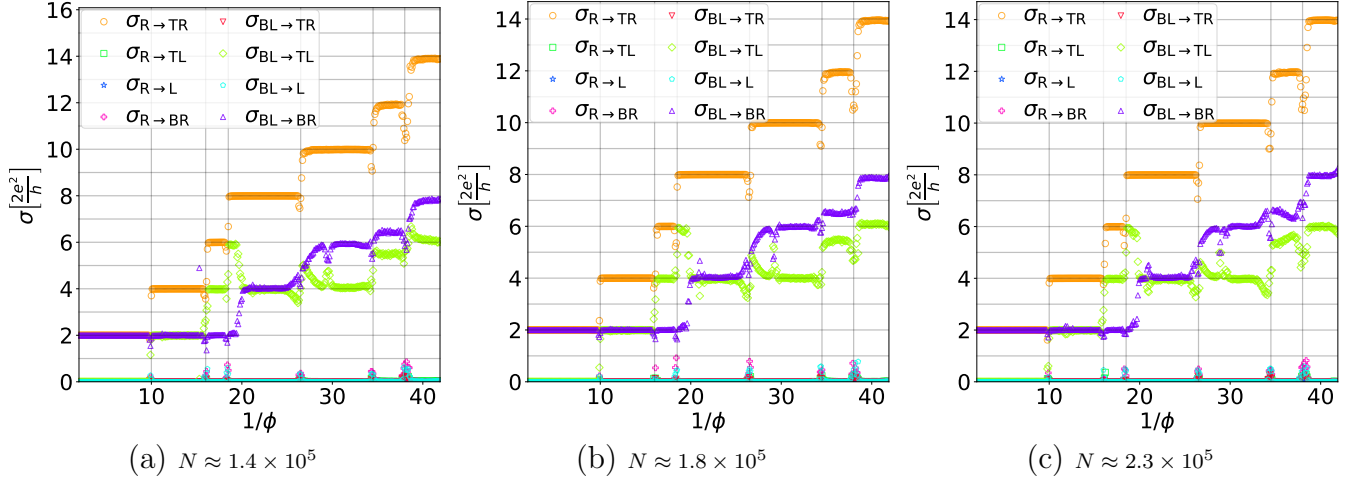


FIG. 16. SLSW Hall bar system finite-size analysis for transmission diagrams, see Fig. 6 for a description of transmission diagrams. The cutoff between the two layers in the LSW is long, $D_C = 4a_0$. The shear width parameter is $L_S = 44$.

For larger $1/\phi$ some features show minor change with system size at plateau transitions. The increases and decreases due to plateau transitions become more localized with larger system size.

3. Tensile layer switching system

A finite-size study for TLSW systems is shown in Fig. 17. Due to the strong fluctuations of $\sigma_{BL \rightarrow TL}$ and $\sigma_{BL \rightarrow BR}$ in TLSW systems, discussing finite-size effects is more difficult than for HLSW and SLSW systems. As for the other system types, the conductance across the first four plateaus is similar for all system sizes. But even for large external magnetic fields, there are differences between Fig. 17b and Fig. 17c close to plateau transitions. In particular the shape of $\sigma_{BL \rightarrow TL}$ and $\sigma_{BL \rightarrow BR}$ differs near

the third plateau. These changes however are fairly small in magnitude and given the satisfactory convergence of all other system types for these system sizes, using either the system size in Fig. 17b or the one in Fig. 17c should be fine for $\phi^{-1} \in [0, 40]$. The existence of finite-size effects for these systems however cannot be ruled out as confidently as for the other system types and finite-size effects should be kept in mind when discussing TLSW systems.

Generically, systems in the regime of 1×10^5 to 2×10^5 sites are sufficient to discuss the first four plateaus of the magnetoconductance and systems of the order 2×10^5 to 3×10^5 are required to discuss the full range of magnetic field shown in the main body of the article. Even for larger plateaus, smaller system sizes should be sufficient to determine generic features of the conductivity shapes, but finite-size effects must be considered if such calculations are discussed.

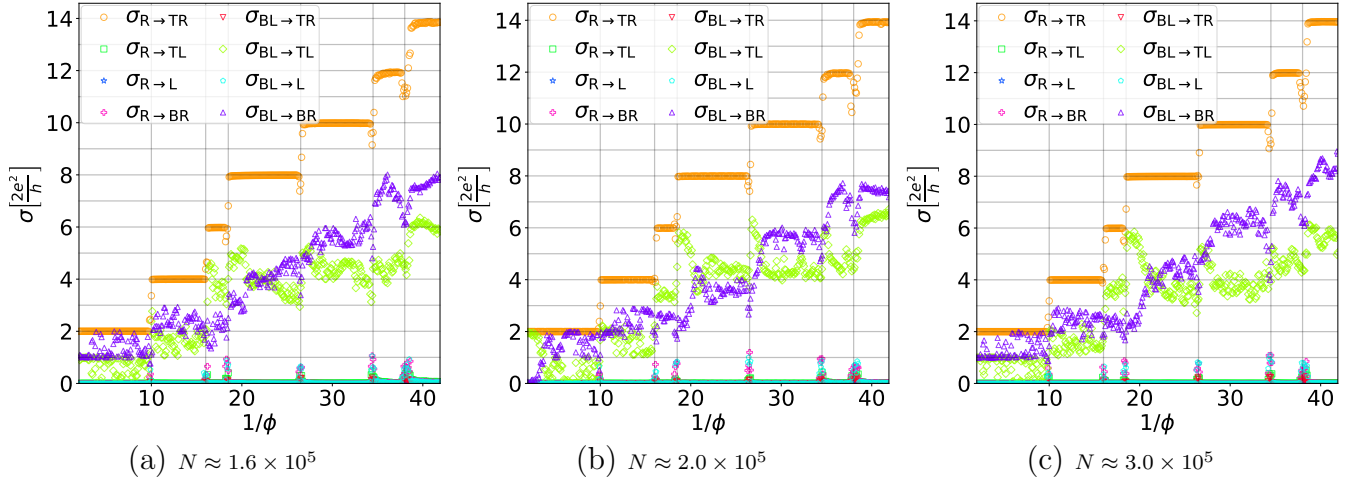


FIG. 17. TLSW Hall bar system finite-size analysis for transmission diagrams, see Fig. 6 for a description of transmission diagrams. The cutoff between the two layers in the LSW is long, $D_C = 4a_0$. The tension length parameter is $L_T = 60$.

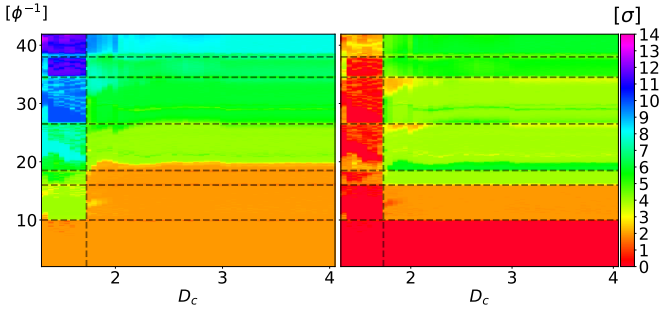


FIG. 18. Parameter study of the cutoff distance D_c for different external magnetic fields ϕ^{-1} for a SLSW system. On the left is $\sigma_{BL \rightarrow BR}$ and on the right is $\sigma_{BL \rightarrow TL}$. The two plots show the conductance in color with the cutoff distance D_c on the y-axis and the magnetic field on the x-axis. The number of sites in the system used for the transmission calculations is $N_C \approx 2.3 \times 10^5$. The shear width parameter is $L_S = 44$.

Appendix B: Numerical cutoff

Another important parameter of the simulation is the cutoff distance D_c . For regular BLG and HLSW systems we chose D_c , such that only nearest-neighbour hopping terms are nonzero. This should be adequate to discuss the IQHE. For twisted bilayer graphene (TBLG) systems and systems with shear and tension however such a short cutoff might not model the physics properly. Thus convergence with respect to D_c should be checked for SLSW and TLSW systems.

1. Sheared layer switching system

In Fig. 18 a calculation of different cutoff distances for SLSW systems is shown. The magnetoconductance shows a large jump at the value $D_c \approx 1.73$ (position of

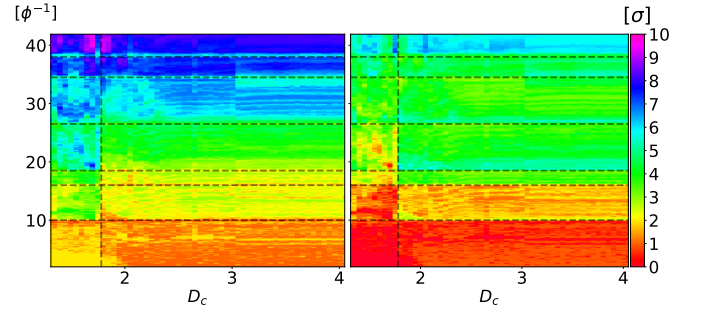


FIG. 19. Parameter study of the cutoff distance D_c for different external magnetic fields ϕ^{-1} for a SLSW system. On the left is $\sigma_{BL \rightarrow BR}$ and on the right is $\sigma_{BL \rightarrow TL}$. The two plots show the conductance in color with the cutoff distance D_c on the y-axis and the magnetic field on the x-axis. The number of sites in the system used for the transmission calculations is $N_C \approx 2.0 \times 10^5$. The tension length parameter is $L_T = 60$.

vertical black line). In the interval $D_c \in [0, 1.73]$, the contribution to $\sigma_{BL \rightarrow BR}$ on the right in Fig. 18 is much larger and the contribution to $\sigma_{BL \rightarrow TL}$ much smaller than to the right of the jump. The dependence on the cutoff distance to the right of the jump is strong and there is no obvious plateau structure for $\sigma_{BL \rightarrow BR}$ in this regime. To the right of the jump, in the interval $D_c \in [1.73, 4.0]$, the magnetoconductance changes less rapidly with D_c and there is a more apparent plateau structure when near the plateau centers of $\sigma_{R \rightarrow TR}$. The magnetoconductance functions show good convergence for values of $D_c > 3.0$. Ultimately the structure of the calculation in Fig. 9 is well converged and a choice of $D_c = 4.0$ is adequate for all presented results.

2. Tensile layer switching system

In Fig. 19 a calculation of different cutoff distances for TLSW systems is shown. Just as for all other calculations, the magnetoconductance for this system type shows much stronger fluctuations than for the SLSW systems. Similarly to the SLSW case, there is a strong jump in the transmission function for a particular value of the cutoff distance. For the TLSW system this value is $D_c \approx 1.78$ (position of vertical black line). The change in transmission however is not as pronounced as in the SLSW case and the plateaus one to four are most affected, whereas the larger plateaus do not exhibit such a jump. There is a strong dependency on D_c in both $\sigma_{BL \rightarrow BR}$ and $\sigma_{BL \rightarrow TL}$ below $D_c \approx 2.3$. After that, there is another minor change in conductance at $D_c = 3.0$, where the decrease due to the fourth plateau transition in $\sigma_{R \rightarrow TR}$ becomes larger. For $D_c \leq 3.0$ however, the magnetoconductance is well converged keeping in mind the usual conductance fluctuations. As such the calculation for $D_c = 4.0$ in Fig. 12 and all other presented results in this paper should be appropriately converged with respect to the numerical hopping integral cutoff D_c .

The strong changes in the structure of the magnetoconductance calculations at particular values of D_c make sense, since they correspond to the inclusion of particular hopping elements in the BLG lattice. In the case of the $D_c \approx 1.7$ jump hoppings between sites of the same sublattice are added respectively.

Appendix C: Other Fermi energies

As mentioned in the discussion of the parameters for all other calculations, the Fermi energy of all systems under consideration was chosen to be $0.95 \text{ eV} \approx 0.35t$. To identify energy dependencies a small study of the Fermi energy is performed for HLSW with fully coupled upper sheet, SLSW and TLSW systems. A small Fermi energy is difficult to investigate, since it requires smaller magnetic fields and thus larger length scales to suppress finite-size effects. Thus a large parameter study of very low-energy properties with a discrete model is currently not feasible due to computing time constraints.

The Fermi energy study is shown in Fig. 20. The first obvious observation for all three system configurations is the difference in the Landau level filling for different Fermi energies. At lower energies and the same magnetic field, fewer bands will be filled and thus an analysis of the same region of magnetic field values at smaller Fermi energies will show a smaller number of plateaus. This is the essential reason why a large Fermi energy was used to perform calculations. To observe larger fillings for smaller energies, one would require smaller magnetic fields and thus larger systems to avoid finite-size effects.

There are changes to the plateau structure of $\sigma_{R \rightarrow TR}$ at different energies, but that is to be expected, since a different underlying band structure at a particular Fermi

energy without magnetic field leads to different plateau transition positions. In particular, the width of the third plateau in $\sigma_{R \rightarrow TR}$ decreases for smaller Fermi energies.

For all three system configurations under consideration the general shapes of $\sigma_{BL \rightarrow BR}$ and $\sigma_{BL \rightarrow TL}$ are remarkably similar for different energies supporting the generality of the discussed results. Although the generic shapes of $\sigma_{BL \rightarrow BR}$ and $\sigma_{BL \rightarrow TL}$ are energy independent, there are also features, that warrant closer inspection.

For the HLSW systems on the left, the conductivities under consideration are largely the same except for two particular structures. The increase of $\sigma_{BL \rightarrow BR}$ and decrease of $\sigma_{BL \rightarrow TL}$ at the transition from fourth to fifth plateau are attenuated for smaller energies. The transition from a smaller peak in $\sigma_{BL \rightarrow BR}$ to a larger one from $E_F = 0.85 \text{ eV}$ to $E_F = 0.9 \text{ eV}$ and finally to $E_F = 0.95 \text{ eV}$ is apparent. There is also a decrease in $\sigma_{BL \rightarrow TL}$ at the transition from second to third plateau for $E_F = 0.95 \text{ eV}$, whose width decreases for $E_F = 0.9 \text{ eV}$ and has entirely vanished for $E_F = 0.85 \text{ eV}$.

For the SLSW systems, the plateau structure is preserved in the range of interest. The conductance $\sigma_{BL \rightarrow BR}$ is shifted to larger ϕ^{-1} for smaller Fermi energies. This causes structure in the conductance $\sigma_{BL \rightarrow TL}$, namely peaks around $\phi^{-1} = 22$ and $\phi^{-1} = 32$, due to the offset between plateau transitions in $\sigma_{R \rightarrow TR}$ and $\sigma_{BL \rightarrow BR}$. The two conductances for the Fermi energy $E_F = 0.95 \text{ eV}$ merely seem to be well aligned such that $\sigma_{BL \rightarrow TL}$ has a plateau structure as well. Thus the monotonous plateau structure in $\sigma_{BL \rightarrow BR}$ is generic for energies in the considered range, but the plateau structure of $\sigma_{BL \rightarrow TL}$ is not. The width change of the third plateau is also reflected in the width of the peak in $\sigma_{BL \rightarrow TL}$ near that transition.

Just as for the previous two system types, the general shape of the conductance calculations is similar for all three energies considered aside from the change in filling due to changed electron density at any particular value of ϕ^{-1} . Like for the HLSW calculations the change in width of the third plateau causes changes in the conductances $\sigma_{BL \rightarrow TL}$ and $\sigma_{BL \rightarrow BR}$. Aside from that the general shape of the conductances is energy independent, but the particular fluctuations do change with energy. For example, the exact structures of $\sigma_{BL \rightarrow TL}$ and $\sigma_{BL \rightarrow BR}$ around the fifth plateau clearly show a small energy dependence. However, the instability of this system type with respect to parameter changes has already been established and this behaviour is not surprising.

For all three system types, changes of features in the region between $\phi^{-1} = 15$ and $\phi^{-1} = 23$ for $E_F = 0.95 \text{ eV}$ coincide with the decrease in the width of the third plateau for smaller Fermi energies. It seems reasonable, that the magnetoconductivity for LSW systems would reflect the changes in the homogeneous systems.

In conclusion, there are changes in the conductivities with Fermi energy. This behaviour however is not unexpected, since the homogeneous system conductance also changes with energy. These changes however do not fundamentally affect the previous discussions of these systems

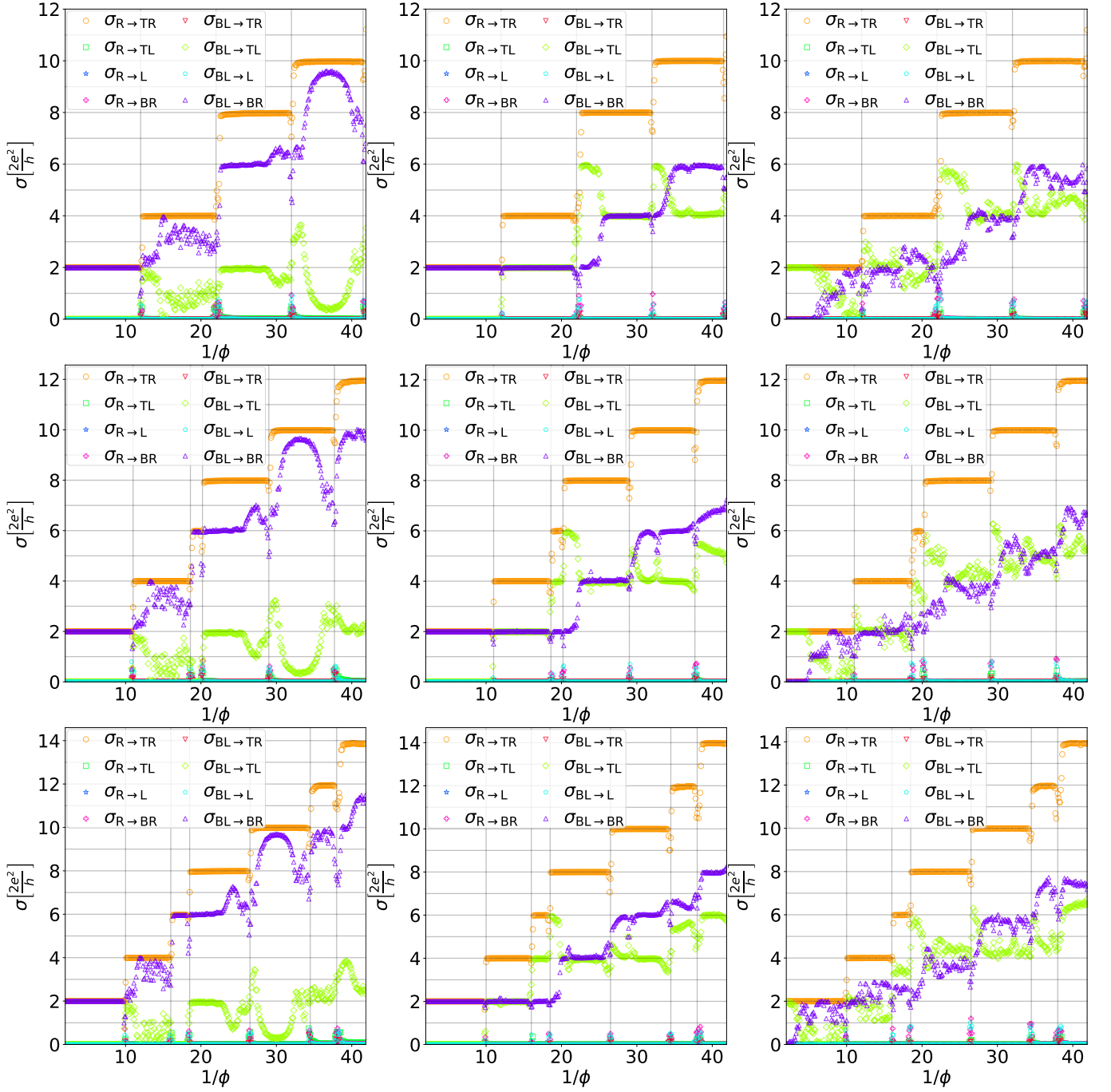


FIG. 20. A study of magnetoconductance for three different Fermi energies. Transmission for HLSW $N \approx 1.6 \times 10^5$ (left), SLSW $N \approx 1.7 \times 10^5$ (middle), TLSW $N \approx 1.8 \times 10^5$ (right) systems. The energies are $E_F = 0.85$ eV (top), $E_F = 0.9$ eV (middle), $E_F = 0.95$ eV (bottom).

and this is a good indicator that the discussed properties

like plateau formation are generic, at least in the energy range investigated.